Journal Name

ARTICLE TYPE

Cite this: DOI: 00.0000/xxxxxxxxxx

Theoretical calculations of the effect of nitrogen substitution on the structural, vibrational, and electronic properties of wolframite-type $ScTaO_4$ at ambient conditions

Lotfi Ibrahim Karaouzène,*[a‡] Tarik Ouahrani,*[a] Ángel Morales-García,[b] and Daniel Errandonea*[c]

Received Date
Accepted Date

DOI: 00.0000/xxxxxxxxxx

In this study, the effect of nitrogen substitution in wolframite-type $ScTaO_4$ was investigated using density-functional theory calculations. First, structural and mechanical properties, as well as the dynamical stability of $ScTaO_4$ were examined deeply for the ambient-pressure structure. Subsequently, we studied how lattice vibrations are affected by hydrostatic pressure and determined the elastic moduli of $ScTaO_4$. The results of our study show that the monoclinic structure of $ScTaO_4$ is rigid and non-compressible. In addition, band-structure calculations show that $ScTaO_4$ has a wide direct band-gap of 4.04 eV, which in turn leads to a possible tuning of electronic properties. We have found that this task can be conducted by partially substituting oxygen atoms in the unit cell with nitrogen atoms. Both band-structure calculations and charge-density analyses revealed a narrowing in the band gap caused by the presence of nitrogen atoms, which act as a shallow acceptor state, resulting in weak repulsive interactions and structural distortions in both Sc and Ta coordination polyhedra; reducing the crystal symmetry from monoclinic to triclinic.

1 Introduction

Among the broad group of ternary oxide compounds, doped and undoped MTO_4 trivalent-metal niobates and tantalates (M = trivalent metal and T = Nb or Ta) are materials with unique and practical properties which favor their use in new green-energy technologies, such as solar cells, solar collectors, and solar fuel reactors. For instance, $InTaO_4$ and $InNbO_4$ have been investigated as efficient photocatalytic materials[1]. Their photocatalytic activity is mainly due to their band-gap values and conduction/valence band levels. However, although the chemical stability of MTO_4 materials is beneficial for many functionalities[2], their poor aqueous solubility and high crystallization temperatures limit the opportunity for soft-chemical routes, as well as frustrate solid-state processing[3]. Nevertheless, despite these difficulties, one way to overcome them is to tailor their properties for specific applications. Building nanoparticles or thin films of these materials by soft chemistry would provide an opportunity for producing them in the amounts required by industry. In this way, applications such as lithium batteries, solid oxide fuel cells, or light-emitting diodes can be assessed[4]. Furthermore, due to their high solubility in water, their reactivity can be an easy tool to engineer their functionalities[5,6].

In contrast to common rare-earth tantalates, the investigations into wolframite-type $ScTaO_4$ (space group: P2/c, Z = 2) are very limited. Few experiments[7–9] have been performed in this compound finding that the material is paramagnetic with a monoclinic structure at zero kelvin but transforms to a ferroelectric phase at a temperature of 280 K[7]. It is also known that $ScTaO_4$ is highly resistant to corrosion at high-temperature[10]. In contrast with these few experimental studies, a detailed theoretical investigation of its stability and bonding properties is still lacking.

On the other hand, recently, Pei *et al.*[11] conducted experiments to investigate the possibility of tuning the properties of the wolframite-type $ScTaO_4$ for water-splitting derived applications. It was discovered that such functionality can be improved by substituting a small fraction of oxygen atoms with nitrogen atoms, which can cause a significant change in the electronic properties. However, detailed information about the percentage of nitrogen substitution was not revealed. These authors hypothesize that their observations could be related to a narrowing of the band gap caused by the chemical substitution of oxygen by nitrogen.

From the theoretical viewpoint, the hypothesis sounds reason-

---

[a] *Laboratoire de Physique Théorique, Université de Tlemcen, BP 119, 13000, Algeria; E-mail: lotfikaraouzene@gmail.com; tarik_ouahrani@yahoo.fr*

[‡] Département de Physique - Faculté des Sciences - Université de Tlemcen, BP 119, 13000, Algeria

[b] *Departament de Ciéncia de Materials i Química Física & Institut de Química Teórica i Computacional (IQTCUB), Universitat de Barcelona, c/Martí i Franquès 1-11, 08028 Barcelona, Spain*

[c] *Departamento de Física Aplicada - Instituto de Ciencia de Materiales, Matter at High Pressure (MALTA) Consolider Team, Universidad de Valencia, Edificio de Investigación, C/Dr. Moliner 50, Burjassot, 46100, Valencia, Spain; E-mail: daniel.errandonea@uv.es*

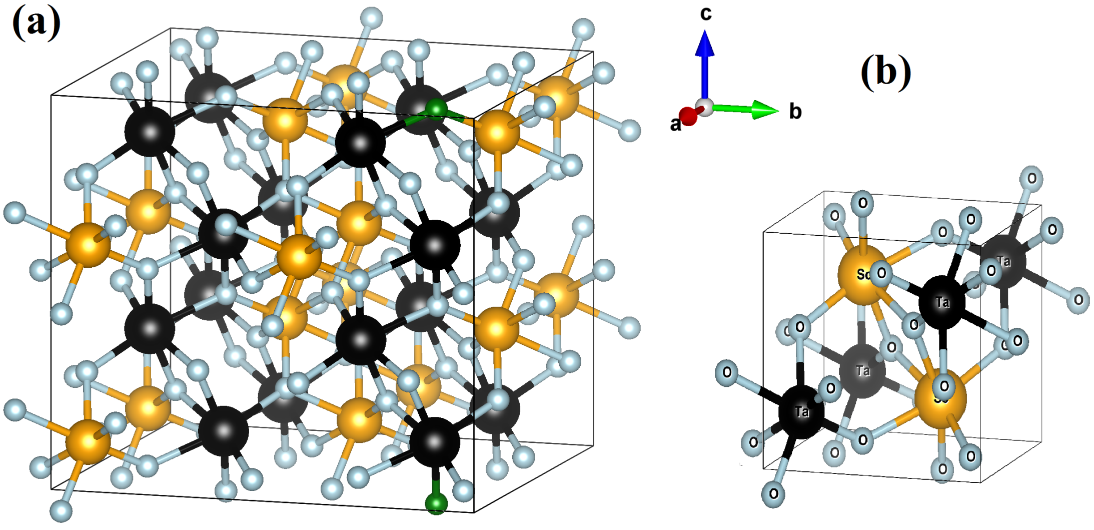

Fig. 1 Crystallographic representation of the 2×2×2 supercell and the conventional unit-cell of $ScTaO_4$.

able because N^{3-} has one electron less than O^{2-} and because of the lower binding energy of the $2p$ states in N in comparison to the in O $2p$ states[12]. However, the insertion of nitrogen in the anionic sub-lattice of the oxide causes the formation of new electronic states that usually fall inside the band gap, not far from the valence band maximum[12]. The additional electron of nitrogen can then act as a shallow acceptor state, able to trigger the onset of a p-type behavior. In this context, it would be interesting to deeply investigate the effect of nitrogen substitution in $ScTaO_4$. Therefore, in the present paper, we intend to analyze in detail the dynamical and mechanical stability as well as the electronic properties of this compound to better understand the behavior shown in the experiments reported by Pei *et al.*[11]. To do this task, we will use the state-of-art density-functional theory (DFT) calculations based on the full potential-linearized augmented plane wave (FP - LAPW) method[13].

This article is outlined as follows: The computational details are briefly summarized in the following Section 2. The results are divided into two subsections containing the analysis of $ScTaO_4$ and N-substituted $ScTaO_4$. The paper ends with the main conclusions of our work.

2 Computational details

Due to our success in treating the d orbital of the scandium atom in other oxides[14], we have carried out the present calculation by means of a full-potential linearized augmented plane wave (FP-LAPW) implemented in the WIEN2K package[13]. The generalized-gradient approximation (GGA) was used for the description of the exchange-correlation energy within the PBEsol prescription[15]. We optimized the Fourier expanded charge density (G_{max}) and the expansion of the non-spherical potential (l_{max}) parameters, which were found to be 14 $(Ry)^{1/2}$ and 10 respectively. The wave functions in the interstitial region were expanded into plane waves with a cutoff of $R_{MT}.K_{max} = 8$. We used very dense meshes, with $N_i = max(1.30 \times |\vec{b}_i| + 0.5)$ defining the number of subdivisions along each reciprocal lattice vector $\vec{b}_i$. As a final consideration, the energy separation between the core states and the valence states was taken as -6 Rydberg, and the self-consistent calculations were judged to have converged to a tolerance of less than 10^{-4} Ry. Additionally, in order to accurately determine the correct band-gap energy for the substituted $ScTaO_4$ compound, we used the Hubbard correction U within the DFT+U method[16]. This empirical correction allows us to overcome the systematic underestimation of the band gap by traditional exchange functionals Furthermore, lattice-dynamics calculations were performed by means of PHONOPY[17] open-source package interfaced to WIEN2K code. This code uses the direct force constant approach (or supercell method)[18,19]. In order to obtain the phonon dispersion curves along with the high-symmetry directions of the Brillouin zone (BZ), we used (2 × 2 × 2) supercells. Integration of the phonon frequencies with a large number of **k**-points (14 × 14 × 14 grid) yielded the phonon density of states (PDOS).

To analyze the covalent and ionic bonding character in our materials, we used the Non-covalent Interactions Index (NCI) as descriptor[20,21], which is calculated using the reduced density gradient of the electron density (ρ), where the density varies gradually. This characterization was carried out within the framework of QTAIM[22,44], as defined by

$$NCI = s = \frac{1}{2(3\pi^2)^{1/3}} \frac{|\nabla\rho|}{\rho^{4/3}} \qquad (1)$$

The 4/3 density exponent guarantees that s is a dimensionless quantity. The properties of $s(\mathbf{r})$ isosurfaces are determined by their critical points[20,21]. The significance of the NCI isosurface is based on the sign of Hessian's second eigenvalue (λ_2) multiplied by the electron density of ρ. If the result is negative, the attractions are judged attractive and the isosurface is colored in blue. However, if it is positive, the attractions are judged repulsive, and the corresponding domains are colored in red. In the

Table 1 Unit-cell parameters (a, b, c, and β angle) and volume at ambient conditions and the bulk modulus and its first pressure derivative of wolframite-type $ScTaO_4$ according to our calculations (Calc) and previous experiments (Expt). The later[7–9,24] are included for comparison.

	a (Å)	b (Å)	c (Å)	V_0(Å^3)	B_0(GPa)	B'_0	β(°)
This work (Calc-PBEsol)	4.806	5.689	5.110	139.64	180	3.00	91.46
Expt[7]	4.807	5.662	5.112	139.09	–	–	91.37
Expt[8]	4.807	5.662	5.112	139.08	–	–	91.62
Expt[9]	4.801	5.673	5.113	139.20	–	–	91.55
Expt[24]	4.809	5.670	5.118	139.55	–	–	91.80

case of $(\lambda_2) * \rho$ is close to zero, weak interactions like van der Waals interactions or hydrogen bonds are invoked, and the isosurfaces are depicted in green.

3 Results and Discussion

3.1 Properties of $ScTaO_4$ and its stability

We accurately relaxed the unit cell of the crystal structure of $ScTaO_4$ using spin-polarized calculations. This is because we expect magnetization when substituting an oxygen atom for a nitrogen atom. We have considered five structures, the conventional cell (shown in Figure 1) to simulate nitrogen substitution of oxygen of 0% (0 N plus 8 O atoms in the unit cell), 12.5% (1 N plus 7 0 atoms), 25% (2N plus 6 O atoms), and 50% (4 N plus 4 O atoms). Further, a 2×2×2 supercell (see Figure 1) has been required to simulate a 1.56% N substitution of oxygen (1 N plus 63 O atoms in the cell). Notice that there are two non-equivalent oxygen sites (See Table 1). However, we found that considering substitution of oxygen by nitrogen in either one or the other site leads to the same results. We will first discuss results from pristine $ScTaO_4$. The aim of this task is to prove the structural, dynamic, and mechanical properties of the studied compound. In the monoclinic structure, the atomic positions, the three lattice parameters, and the β angle have been optimized. Our results are summarized in Tables 1 and 2. As it can be seen in the tables, the GGA-PBEsol calculations describe reasonably the crystal structure of wolframite-type $ScTaO_4$.

In order to explore the response of $ScTaO_4$ to hydrostatic pressure, we have fit the calculated energy-volume (E,V) curve with a third-order Birch-Murnaghan equation of state (EOS)[25]. The obtained equilibrium volume (V_0), bulk modulus (B_0), and its derivative (B'_0) are listed in Table 1. The calculated bulk modulus, 180 GPa, is around 20 % smaller obtained from acoustic velocity measurements in polycrystalline $ScTaO_4$[26]; B_0 = 227 GPa. We believe our result is the most accurate because it is within the values predicted by crystal chemistry for wolframite-type tantalates[27]. Another argument in favor of our calculated bulk modulus is that it is very similar to that of isomorphic $InTaO_4$, with B_0 = 171–179 GPa[28] and fergusonite-type $YTaO_4$ with B_0 = 128–183 GPa[29,30]. Anyway, in spite of the small differences in the value of the bulk modulus, our and the previous study[26] support that $ScTaO_4$ is much less compressible than wolframite-type tungstates, molybdates, and vanadates[27].

Next, we analyze the dynamical properties. The frequencies of the normal modes have also been obtained from the diagonalization of the dynamical matrix. The phonon dispersion curve and phonon density of states (DOS) are plotted in Figure 2. As the plot does not show any imaginary mode, we can state the dynamical stability of $ScTaO_4$ in the wolframite structure at ambient conditions. Similar results have been obtained from calculations carried out under a hydrostatic pressure of 5 GPa, supporting the dynamical stability of such compound up to this pressure. We have also calculated the active frequencies of Raman (R) and infrared (IR) modes and the corresponding mode-symmetry assignment.

Table 2 Calculated atomic coordinates of monoclinic wolframite-type $ScTaO_4$ (space group P2/c) at ambient pressure compared with results from experiments[24] which are given between brackets. The Wyckoff positions are also given.

atom	*x*	*y*	*z*
Sc(2f)	0.5 (0.5)	0.32382 (0.322)	0.25 (0.25)
Ta(2e)	0 (0)	0.82364 (0.826)	0.25 (0.25)
O_1(4g)	0.21726 (0.213)	0.10765 (0.102)	0.43400 (0.438)
O_2(4g)	0.26596 (0.265)	0.38374 (0.383)	0.90539 (0.902)

Group-theory considerations of the wolframite structure yield 23 optical modes and 3 acoustic modes at the center of the Brillouin zone (Γ-point). All the phonon branches are displayed in Figure 2. The obtained mode frequencies of optical modes and the symmetry assignment are summarized in Table 3. The analysis of the zone center phonons gives the following mechanical decomposition: $\Gamma = 8A_g + 8A_u + 10B_g + 10B_u$. $\Gamma_{acoustic} = A_u + 2B_u$, whereas, $\Gamma_{optic} = 8A_g(R) + 7A_u(IR) + 10B_g(R) + 8B_u(IR)$.

In a previous study, only twelve of the Raman-active modes have been measured[26]. Their frequencies are compared with our calculations in Table 3. Calculations and experiments agree within 10 % which is typical for DFT calculations in ternary oxides[28,31]. Interestingly the distribution of Raman modes in $ScTaO_4$ resembles that of $InTaO_4$[27]. In particular, that are three high-frequency Raman modes and four high-frequency IR modes, with wavenumbers higher than 600 cm^{-1} that are "isolated" from the rest of the modes. In wolframite-type compounds, as a first approximation, the vibrational modes can be classified as internal and external modes with respect to the TaO_6 octahedra[27]. The internal modes correspond to normal motions of atoms inside the TaO_6 octahedra, while the external modes involve motions of them as rigid units against the Sc atoms.

The phonon frequencies of the internal modes are higher than those of the external modes. In particular, from our calculations, we can state that the two Raman modes of $ScTaO_4$ with the high-

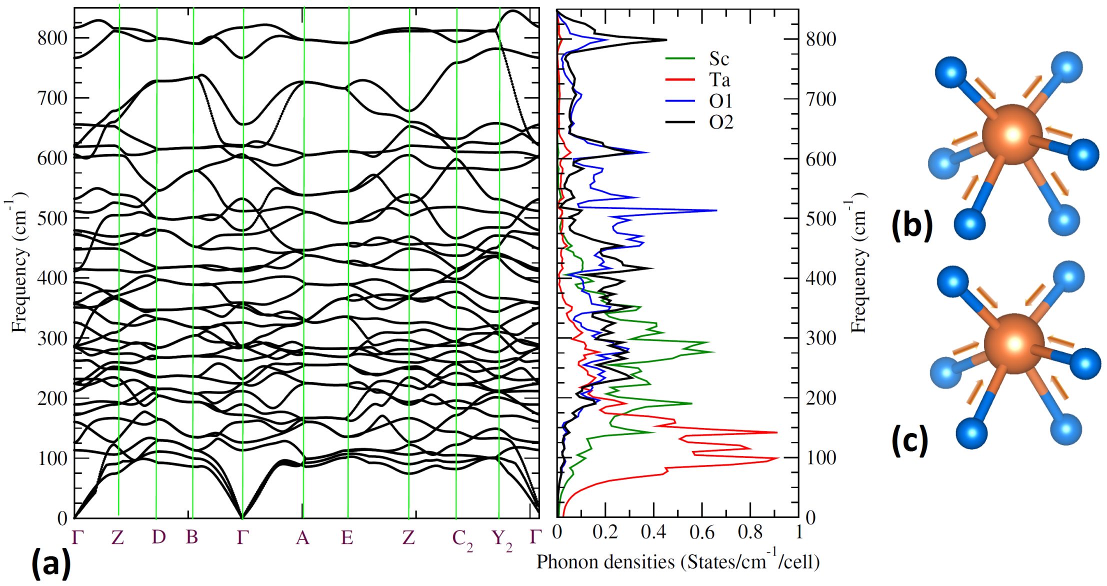

Fig. 2 (a) Phonon dispersion (left) and phonon density of states (DOS) curves (rigth) of $ScTaO_4$ at zero pressure. The partial densities of states (PDOS) projected onto Sc, Ta, O1 and O2 are also presented with green, red, blue, and black colors, respectively. (b) and (c) representation give respectively the phonon eigenvectors of asymmetric B_g and symmetric A_g modes in the TaO_6 octahedron.

Table 3 Calculated Raman (R) and infrared (IR) frequencies (ω) at 0 GPa (in cm^{-1}), linear pressure coefficients (dω/dP) (in cm^{-1}/GPa) and Grüneisen parameter (γ), dimensionless. Raman frequencies are compared with experimental frequencies (ω_{exp}) reported by Cheng et al.[26].

Raman					IR			
Mode	ω	dω/dP	γ	ω_{exp}	Mode	ω	dω/dP	γ
B_g(R)	113.2	0.54	0.86	120	B_u(IR)	172.1	-2.81	-2.94
A_g(R)	126.2	0.22	0.31	140	B_u(IR)	211.5	-0.76	-0.65
B_g(R)	160.2	0.18	0.20	180	B_u(IR)	224.5	-0.64	-0.51
B_g(R)	189.3	-0.19	-0.18	200	A_u(IR)	231.9	1.78	1.38
B_g(R)	223.8	0.77	0.62	240	B_u(IR)	284.5	5.19	3.28
A_g(R)	262.3	-0.49	-0.34		A_u(IR)	286.5	0.33	0.21
A_g(R)	285.2	2.34	1.48		A_u(IR)	325.9	0.13	0.07
B_g(R)	287.3	0.69	0.43	300	B_u(IR)	350.9	4.55	2.34
B_g(R)	356.4	3.66	1.85		A_u(IR)	411.3	4.95	2.17
A_g(R)	359.1	3.14	1.57	380	B_u(IR)	447.5	6.89	2.77
B_g(R)	392.7	5.66	2.60		B_u(IR)	479.2	3.65	1.37
A_g(R)	415.4	2.59	1.12	430	A_u(IR)	531.9	4.90	1.66
B_g(R)	472.3	4.09	1.56	500	B_u(IR)	600.7	5.73	1.72
A_g(R)	511.3	4.08	1.44	530	A_u(IR)	605.7	5.62	1.67
B_g(R)	618.5	5.99	1.74		A_u(IR)	766.4	4.37	1.03
A_g(R)	621.0	4.70	1.36					
B_g(R)	655.8	6.13	1.68	650				
A_g(R)	816.9	5.32	1.17	842				

est frequencies (one A$_g$ and B$_g$) can be associated with internal symmetric and asymmetric stretching vibrations of the TaO$_6$ octahedron. The atomic movements associated to these two modes can be seen in Fig. 2. Notice that the A$_g$ mode has a very similar frequency in ScTaO$_4$ (817 cm^{-1}) and InTaO$_4$ (804 cm^{-1})[28]; both modes have also a similar pressure coefficient (5.32 cm^{-1}/GPa and 4.95 cm^{-1}/GPa, respectively). These observations are fully consistent with the assignment of the highest frequency Raman mode to an internal stretching vibration of the TaO$_6$ octahedron. From our calculations we have also concluded that the movements of oxygen atoms dominate most of the vibrations at frequencies above 400 cm^{-1}. We have also computed the vibrational modes at high-pressure up to a pressure of 5 GPa. We have found that all modes follow a linear behavior with pressure. The calculated pressure coefficients are provided in Table 3, together with the corresponding mode Grüneisen parameters $\gamma = (B_0/\omega)\times(\mathrm{d}\omega/\mathrm{dP})$, which describe the effect that changing the volume of a crystal lattice has on its vibrational properties. Grüneisen parameters have been computed using B_0 = 180 GPa. We have found that, as expected, most modes harden under compression. However, there are five modes (three IR and two Raman) with negative pressure coefficients. All of them are external modes. In particular, one IR mode, the B$_u$ mode with wavenumber 172.1 cm^{-1}, undergoes an important softening under compression. The existence of this mode suggests that crystal instabilities are expected to develop beyond 5 GPa, triggering a structural phase transition[32].

Next, we deal with the calculations of elastic stiffness ($\mathbb{C}_{ij}$). Their analysis provides information about bonding characteristics, mechanical and structural stability, and elastic moduli. By diagonalizing the $\mathbb{C}_{ij}$ matrix, which has thirteen elements different than zero, we have evaluated the Born stability criteria[33] which enables us to determine the elastic stability of the crystal. For a monoclinic system, they are:[34,35]:

$$C_{11} > 0, C_{22} > 0, C_{33} > 0, C_{44} > 0, C_{55} > 0, C_{66} > 0,$$

$$(C_{11} + C_{22} + C_{33} + 2C_{12} + 2C_{13} + 2C_{32}) > 0,$$

$$(C_{33}C_{55} - C_{35}^2) > 0, (C_{44}C_{66} - C_{46}^2) > 0,$$

$$(C_{22} + C_{33} - 2C_{23}) > 0,$$

$$\left[C_{22}(C_{33}C_{55} - C_{35}^2) + 2C_{23}C_{25}C_{35} - C_{23}^2C_{55} - C_{25}^2C_{33}\right] > 0,$$

$$\begin{aligned} &2[C_{15}C_{25}(C_{33}C_{12} - C_{13}C_{23}) + C_{15}C_{35}(C_{22}C_{13} - C_{12}C_{23}) + \\ &C_{25}C_{35}(C_{11}C_{23} - C_{12}C_{13})] \\ &-[C_{15}^2(C_{22}C_{33} - C_{23}^2) + C_{25}^2(C_{11}C_{33} - C_{13}^2) + \\ &C_{35}^2(C_{11}C_{22} - C_{12}^2)] + C_{55}(C_{11}C_{22}C_{33} - C_{11}C_{23}^2 - C_{22}C_{13}^2 - \\ &C_{33}C_{12}^2 + 2C_{12}C_{13}C_{23}) > 0 \end{aligned}$$

The calculated elastic constants are given in Table 4. It is to be noticed that the mechanical stability conditions involving the elastic constants in the above-given equations are all satisfied. Thus, the wolframite structure is mechanically stable. In the Table 4, it observed that C_{11}, C_{22}, and C_{11} are larger than other elastic constants. This indicates that axial compression requires larger forces than shear and tensile deformations. From the elastic constants, we can use ELATE tool[36] to calculate the bulk (K), Young (E), and shear (G) moduli within the Voigt (V)[37], Reuss (R)[38], and Hill (H)[39] approximations. We have found that $K > E > G$ in agreement with our previous conclusion. The obtained values for the bulk modulus agree with the value obtained from the Birch-Murnaghan EOS (180 GPa). On the other hand, the bulk modulus is much larger than the shear modulus. According to Pugh's criteria[40], the ratio B/G can be regarded as an index of the elastic characteristics of materials. The critical B/G value for ductile and brittle materials is 1.75. In our case, $B/G > 2.27$, which indicates that ScTaO$_4$ is ductile.

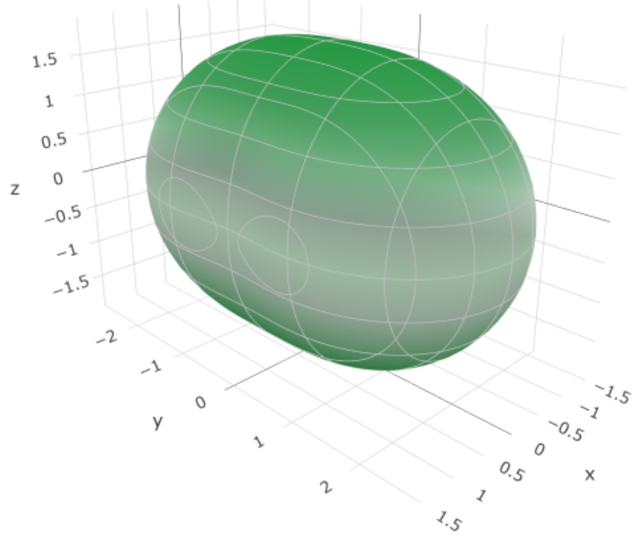

Fig. 3 Directional dependence of the linear compressibility of ScTaO$_4$ at ambient pressure. Units of axes are 10^{-3} GPa^{-1}.

The compound also shows a clear anisotropy along the **b** direction. The linear compressibility is estimated at 1.76 × 10^{-3} GPa^{-1}, which stipulates that the compound is sensible to the directional compression along the **b** axis. A plot of the directional dependence of the linear compressibility is presented in Figure 3 confirms this tendency. This conclusion is compatible with results obtained from high-pressure X-ray diffraction (XRD) in wolframite-type InTaO$_4$[28]. Further, the fact that C$_{11}$ and C$_{11}$ + C$_{12}$ > C$_{33}$ indicates that the bonding force and tensile modulus of elasticity are greater in the (001) direction along the **c**-axis. This indicates that the shear strain is easier than the linear compression along the **a** and **c** crystallographic axes[41].

To conclude the description of ScTaO$_4$ at ambient pressure, we will next discuss the electronic properties of ScTaO$_4$. Optical-absorption experiments has been done in wolframite-type InTaO$_4$ compound[28]. The reported band-gap energy is 3.79 (5) eV. For ScTaO$_4$ we have determined the band-gap energy from band

Table 4 Calculated elastic constants ($\mathbb{C}_{ij}$ in GPa) of wolframite-type $ScNbO_4$. Bulk modulus (K), Young modulus (E) and shear modulus (G) calculated using the Voigt (V), Reuss (R), and Hill (H) approximations. Units are GPa.

C_{11}	C_{12}	C_{13}	C_{15}	C_{22}	C_{23}	C_{25}	C_{33}	C_{35}	C_{44}	C_{46}	C_{55}	C_{66}
264.18	134.28	137.51	5.17	237.00	95.81	-14.63	295.55	19.20	70.98	-15.16	93.22	66.77
K_V	K_R	K_H	E_V	E_R	E_H	G_V	G_R	G_H				
170.22	167.78	169.00	195.74	183.56	189.67	74.80	69.65	72.23				

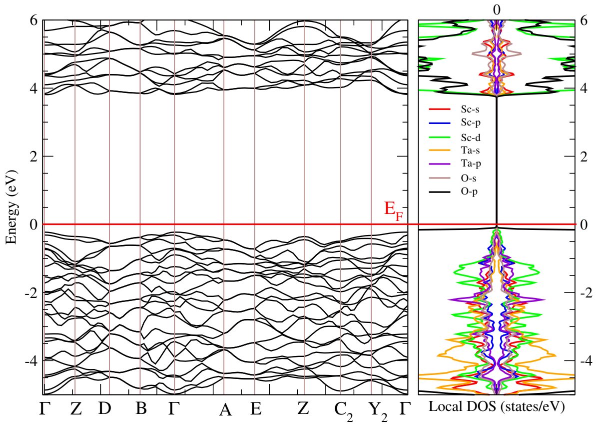

Fig. 4 Right: Band structure and left : density of states of spin (up) and spin (down) for $ScTaO_4$ pristine compound.

structure calculations. The band structure is provided in Figure 4, which also includes the electronic DOS. A quick glance at the figure reveals that the $ScTaO_4$ has a direct band gap in the Γ point. The band gap is estimated to be 4.04 eV, which is similar to the value found for $InTaO_4$. Further, from the UV-vis diffuse reflectance spectra measured by Pei et al.[11] in N-substituted $ScTaO_4$ it can be extrapolated that in $ScTaO_4$ the conduction-band minimum (CBM), and valence-band maximum (VBM) are located between around ∼-0.18 and ∼ 3.75 eV, respectively. Thus, a value of 3.95 eV is estimated for the band-gap energy, which agrees with our finding. In our calculations, the band structure shows a paramagnetic behavior, with a dense electronic level near the Fermi level. The analysis of orbital occupation at ambient pressure has also been done using the electronic partial DOS (see Figure 4). In the plot of the electronic DOS, we have taken care to show the contribution of orbital projection in the range of -5 to 6 eV. Because $ScTaO_4$ is of the d^0 type, we can see that the majority of the orbitals near the Fermi level are governed primarily by *p* orbitals from oxygen atoms. However, we can also note a non-negligible hybridization of these states with the electron of Ta-*d* orbitals.

3.2 The effect of nitrogen substitution in the properties of $ScTaO_4$

After having analyzed the stability and the vibrational. mechanical, and electronic properties of pristine $ScTaO_4$, we will now deal with the effect of the partial nitrogen substitution of the oxygen atoms. To figure out the effect of this substitution, we plotted in Figure 5, the partial density of states of 0%, 1.56%, 12.5%, 25%, and 50% nitrogen substitution. The effect of substitution on the band gap is sizeable. The plot depicts an accumulation of 2*p* orbitals of nitrogen atoms below the Fermi level. In fact, the nitrogen atoms substituting oxygen atoms behave as impurities in the diamagnetic oxide matrix, bringing about a spin magnetic moment which may in principle originates collective magnetic properties in pristine $ScTaO_4$. Furthermore, at a concentration of 25%, the 2*p* nitrogen level overlaps with the Fermi level due to Hund's rule coupling[42]. Additionally, we have found an increase in the magnetic moment from 0.5 to 1.5 μ_B when going from 1.56% to 50% nitrogen substitution by the use of PBEsol+U method. The most stable configuration of this compound is found with spin polarization, indicating that this solution is more stable than the non-spin-polarized. Note that such identification is important because the structural and electronic properties are different. Further analysis is required to identify the magnetic structure with the minima energy by analyzing different spin configurations. Fortunately, this has a minor impact on the structural and electronic properties given the similar energy of different spin configurations.

By introducing a Hubbard correction (U), we can shift these orbitals beyond the Fermi level (see Figure 6). Here, we have used a value of U = 4.57 eV for Sc-*d*[14], and for each concentration of nitrogen substitution, we have varied the U from 1.2 to 2 eV for the N-2*p* atom[43]. Notably, the attempt to apply such a correction leads to varying the position of 2*p*-N states of the minority spin channel into the valence band. With the aid of this correction, our GGA-PBEsol+U calculations estimate band-gap values of E_g = 2.75, 2.50, 2.0, 1.75, and 1.4 eV, respectively, in good agreement with the experimental evidence reported by Pei et al.[11]. Thus, the delocalization of N orbitals is the main cause of the band-gap reduction in N-substituted $ScTaO_4$.

On general grounds, the changes in the electronic band structure are in fact accompanied by a small increase in the unit-cell volume (compared to $ScTaO_4$) and a distortion of the crystal structure which during optimization reduces the symmetry from monoclinic to triclinic. In Table 5 we provide the unit-cell parameters obtained for different percentages of N substitution.

To understand the distortion of the crystal structure, we will discuss, as an example, the $ScTaO_4N$ (25% N) structure to discuss the possible origins of the structural distortion. We have analyzed the changes in structural, bonding, and vibrational properties. The spin density, electron localization function (ELF), and a reduced gradient of the electron density (*s*) have been used to test the possibility of the electronic origin of distortion. All these approaches are based on the topology of electron density[22,44]. Figures 7(a), 7 (b) and 7 (c) depict three-dimensional isosurfaces

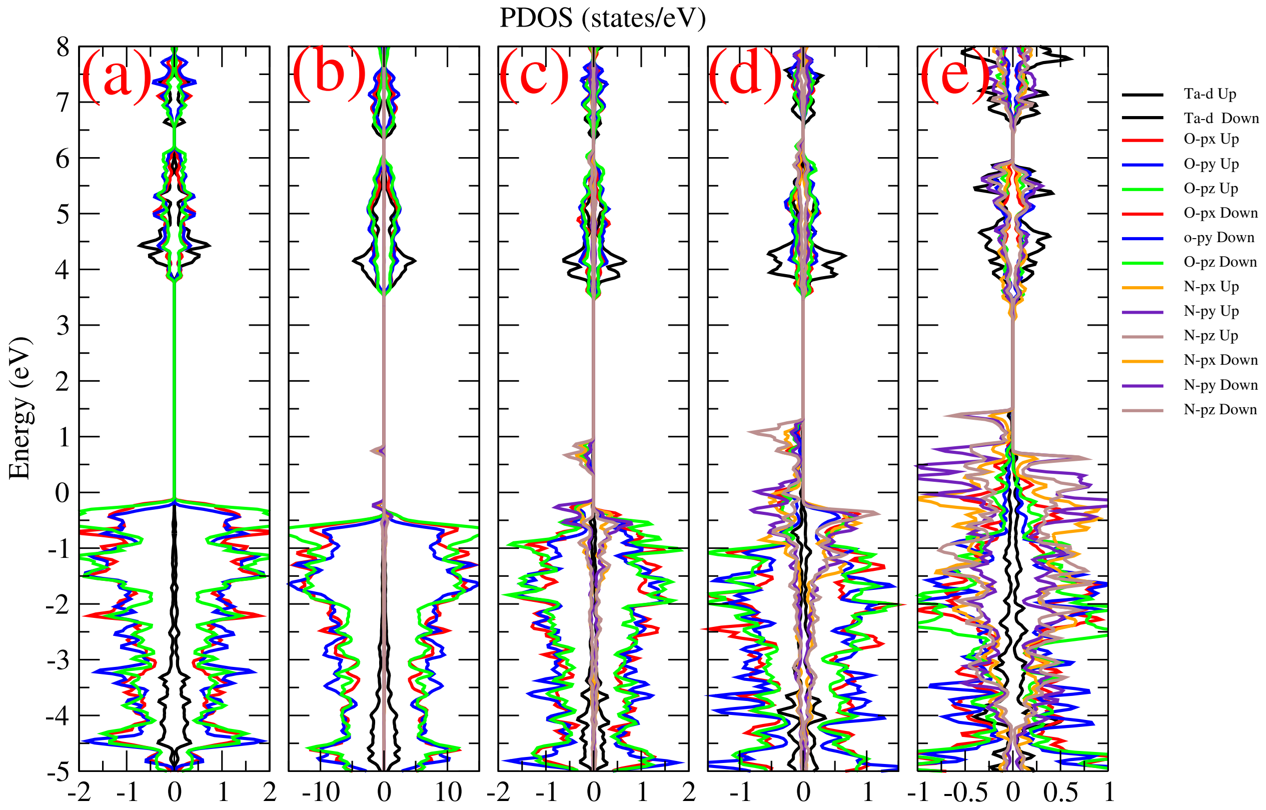

Fig. 5 Spin-resolved partial electronic DOS for the $ScTaO_{1-x}N_x$. The plots correspond to (a) 0.0%, (b) 1.56%, (c) 12.5%, (d) 25%, and (e) 50% of nitrogen substitution.

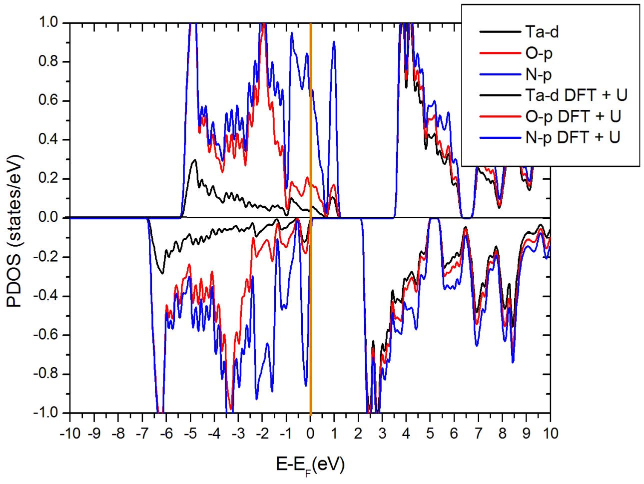

Fig. 6 Partial density of state of the Ta, O, and N atoms. In the upper plot, we show the spin-down channel without the DFT+U correction and at the bottom with the U correction. The plot is done for a concentration of 25% of nitrogen substitution, here U= 1.7 eV

Table 5 Calculated lattice parameters, angles, and unit-cell volume of optimized $ScTaO_{4-x}N_x$ compounds. The a, b, c parameters are in (Å) and volume in (Å^3). N/O gives the percent of oxygen atoms substituted by nitrogen.

N/O	a	b	c	α	β	γ	volume
1.56%	4.84	5.75	5.15	90.01	91.31	90.15	143.29
12.5%	4.86	5.73	5.16	90.11	90.71	90.89	143.56
25%	4.86	5.76	5.13	90.56	89.82	91.77	143.53
50%	4.87	5.84	5.06	90.00	92.51	90.00	143.77

of spin density, ELF, and the reduced gradient s. The three plots clearly show that the substitution of the oxygen atom by the nitrogen induces an excess of electrons on the N atoms. The substitution of an O atom by another anion with an extra electron, such as the nitrogen atom in the d^0-$ScTaO_4$ compound, involves the movement of the Ta and Sc cations from the center of their coordination octahedra toward the N^{3-} donor atom, changing the symmetry of the crystal structure from P2/c to P$\bar{1}$. The reduced gradient plot shows that the additional electron gives rise to strong repulsive interactions, showing in the red isosurface[45]. The spin density and ELF isosurface gathered in both Figures 7(a), 7(b) indicate that the extra electron is stronger in Sc–N bonds than in Ta–N bonds.

Assuming that the substitution mechanism involves the formation of new bands close to the Fermi level, the result indicates the possibility of spontaneous hybridization between N- and O-

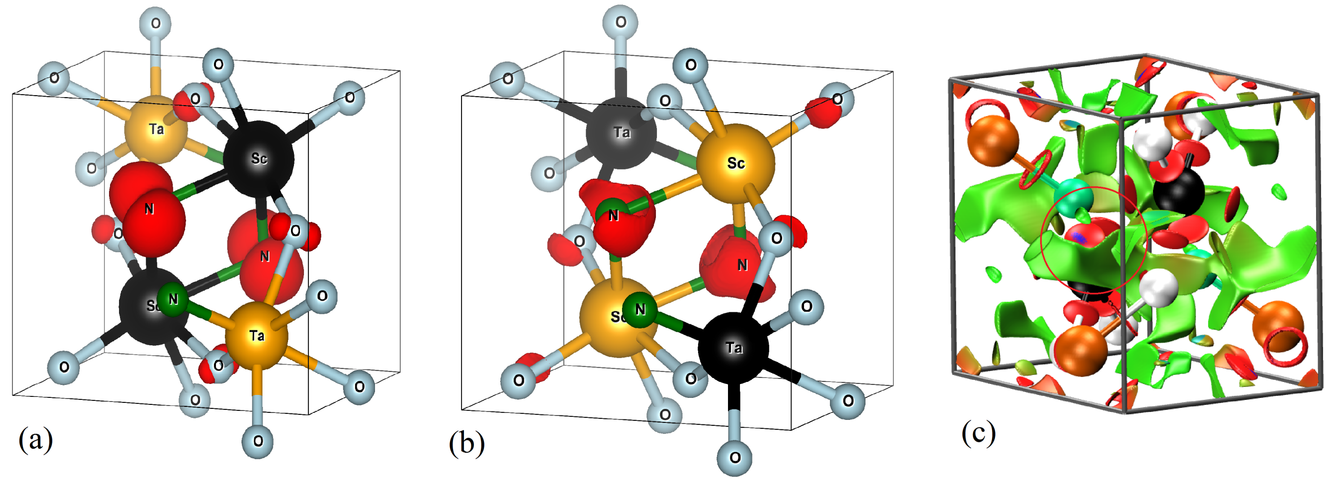

Fig. 7 (a) Spin density, (b) ELF, and (c) reduced gradient of the electron density (s) isosurfaces.

Table 6 Calculated (ω) Raman (R) and infrared (IR) modes of triclinic $ScTaO_3N$ structure (25% N $ScTaO_4$).

Raman		IR	
Mode	ω (cm^{-1})	Mode	ω (cm^{-1})
A_g(R)	105.0	A_u(IR)	150.1
A_g(R)	137.1	A_u(IR)	172.6
A_g(R)	174.0	A_u(IR)	198.9
A_g(R)	204.6	A_u(IR)	217.9
A_g(R)	219.3	A_u(IR)	275.2
A_g(R)	262.3	A_u(IR)	289.2
A_g(R)	265.4	A_u(IR)	295.5
A_g(R)	312.9	A_u(IR)	318.8
A_g(R)	353.3	A_u(IR)	391.3
A_g(R)	378.5	A_u(IR)	437.5
A_g(R)	393.8	A_u(IR)	482.8
A_g(R)	456.6	A_u(IR)	498.9
A_g(R)	486.0	A_u(IR)	589.6
A_g(R)	602.8	A_u(IR)	604.2
A_g(R)	608.5	A_u(IR)	761.6
A_g(R)	648.2		
A_g(R)	800.5		
A_g(R)	862.1		

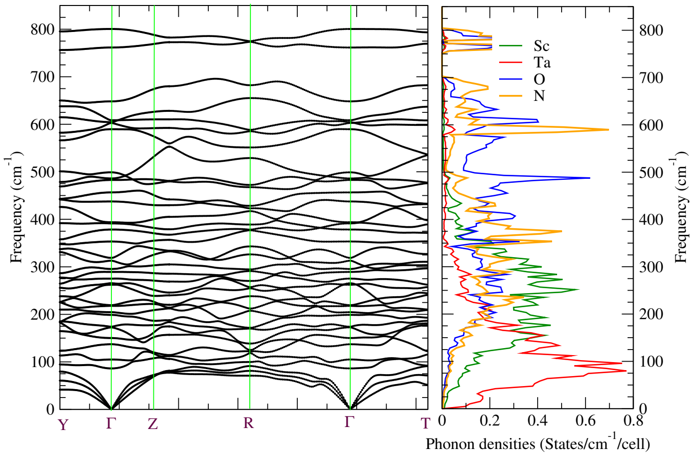

Fig. 8 Phonon dispersion and phonon density of states curves of P$\bar{1}$ $ScTaO_3N$ structure. The partial DoS (PDoS) projected onto Sc, Ta, O and N are also presented with green, red, blue, and orange respectively.

2p and Ta-d bands that leads to the different symmetry characters. Therefore, a hybridization of this type would correspond to a charge density that breaks the monoclinic lattice symmetry. Due to the fact that the electronic instability could trigger structural instabilities, we calculated the phonon dispersion of the N substituted structure. The phonon dispersion of the triclinic distorted structure (P$\bar{1}$) is shown in Figure 8. The plot shows that the triclinic structure is dynamically stable. Thus, the transformation toward the new ground state and energetically favored structure results from a weak structural distortion which accommodates the excess of charge of N. The triclinic structure point group is C_i(-1) and also has 36 modes with the mechanical decomposition : $\Gamma_{acoustic} = 18A_g + 18A_u$, in which $\Gamma_{acoustic} = 3A_u$ and $\Gamma_{optic} = 18A_g + 15A_u$. The infrared and Raman modes of the P$\bar{1}$ structure are gathered in Table 6. Interestingly the phonon distribution is very similar for N-substituted and pristine $ScTaO_4$. In particular, the internal high-frequency modes of the TaO_6 octahedron are little affected by N substitution. This is consistent with the fact that the triclinic structure is a gradual distortion of wolframite.

4 Conclusions

We have performed a density-functional study of $ScTaO_4$. The crystal structure, as well as the mechanical, vibrational, and electronic properties, have been characterized. A comparison with experimental evidence supports our conclusions. In particular, we have found that $ScTaO_4$ is an incompressible material with a direct band-gap energy of 4.04 eV. In addition, we have reported all Raman- and IR-active modes and their symmetry and pressure coefficients. Subsequently, in an attempt to disclose the effect of nitrogen substitution shown by the experiments conducted recently by Pei *et al.*[11], we have used five structures with different levels of substitution of oxygen by nitrogen. The results show that the nitrogen atoms substituting oxygen atoms play the role of a hole acceptor near the Fermi level. The extended electron distribution of the N^{3-} anion generates these states. Furthermore, to shift the 2*p* N states beyond the Fermi level, we used a Hubbard correction, which allowed us to approach the experimental band gap found by Pei *et al.*[11]. A bonding analysis has shown that the nitrogen substitution creates a distortion that originates from a change in electronic population in both the Ta and Sc octahedral units. This later enhances the repulsive distortion in the unit cell, resulting in a subtle monoclinic-triclinic structural distortion.

Data availability

All relevant data are available from the corresponding author upon reasonable request.

Credit authorship contribution statement

Lotfi Ibrahim Karaouzene: Investigation, original draft, Writing - review & editing **Tarik Ouahrani**: Conceptualization, Formal Analysis, Writing - review & editing, **Ángel Morales-García** Writing - review & editing, **Daniel Errandonea** : Conceptualization, Formal Analysis, Writing - review & editing, Resources, Supervision.

Declaration of competing interest

The authors declare that they have no known competing financial interests or personal relationships that could have appeared to influence the work reported in this paper.

Acknowledgements

L.I.K. acknowledges the financial support given by the Laboratory of Theoretical Physics of the University of Tlemcen. D.E. thanks the financial support from Generalitat Valenciana under Grant PROMETEO 2018/123-EFIMAT and by the Spanish Ministerio de Ciencia, Universidades, e Investigación under grants PID2019-106383GB-41 and RED2018-102612-T (MALTA Consolider network). A. M.-G. thanks the support by the Spanish MICIN through the projects PID2020-115293RJ-I00/AEI/10.13039/501100011033 and Spanish MICIUN/FEDER RTI2018-095460-B-I00, and Marìa de Maeztu MDM-2017-0767 grants.

AUTHOR INFORMATION

ORCID
Daniel Errandonea: 0000-0003-0189-4221
Tarik Ouahrani: 0000-0002-1315-7870
Ángel Morales-García: 0000-0003-0491-1234

Notes and references

1 Z. Zou, J.Ye and H. Arakawa, *Int. J. Hydrogen Energ.*, 2003, **28**, 663–669. http://doi.org/10.1016/S0360-3199(02)00159-3

2 K. Shimizu, S. Itoh, T. Hatamachi, T. Kodama, M. Sato and K. Toda, *Chem. Mater.*, 2005, **17**, 5161–5166. https://doi.org/10.1021/cm050982c

3 V. Thangadurai, S. Adams and W. Weppner, *Chem. Mater.*, 2004, **16**, 2998–3006. https://doi.org/10.1021/cm031176d

4 M. Nyman, M. A. Rodriguez, L. E. Shea-Rohwer, J. E. Martin and P. P. Provencio, *J. Am. Chem. Soc.*, 2009, **131**, 11652–11653. https://doi.org/10.1021/ja903823w

5 S. Omwoma, W. Chen, R. Tsunashima and Y. F. Song, *Coordin. Chem. Rev.*, 2014, **13**, 1518–1525. http://doi.org/doi:10.1016/j.ccr.2013.08.039

6 A. Enferadi-Kerenkan, T.-O. Do and S. Kaliaguine *Catal. Sci. Technol.*, 2018, **8**, 2257–2284. https://doi.org/10.1039/C8CY00281A

7 W. L. Zhong, P. L. Zhang and H. C. Chen, *Solid State Commun.*, 1984, **49**, 467-469. https://doi.org/10.1016/0038-1098(84)90665-3

8 D. Elwell, W. L. Kway and R. S. Feigelson, *J. Cryst. Growth.*, 1985, **71**, 237-239. https://doi.org/10.1016/0022-0248(85)90069-7

9 L. H. Brixner, *J. Chem. Educ.*, 1980, **57**, 588-590. https://doi.org/10.1021/ed057p588

10 F. Ye, Y. Yuan, S. Yan, L. Guo and J. Yu, *Mater. Chem. Phys.*, 2020, **256**, 123679. https://doi.org/10.1016/j.matchemphys.2020.123679

11 L. Pei, H. Cai, H. Jin, T. Li, H. Zhu, Y. Yuan, J. Zhong, S. Yan and Z. Zou, *ChemCatChem.*, 2021, **13**, 180-184. https://doi.org/10.1002/cctc.202001341

12 J. C. Slater, *Quantum Theory Of Atomic Structure*, McGraw-Hill, New York, 1960.

13 P. Blaha, K. Schwarz, G.K.H. Madsen, D. Kvasnicka and J. Luitz, in *WIEN2K, An Augmented Plane Wave Plus Local Orbitals Program for Calculating Crystal Properties*, ed. K. Schwarz, Vienna Technological University, Austria, 2001.

14 T. Ouahrani, F.-Z. Medjdoub, S. Gueddida, A. L. Fernandez, R. Franco, N.-E. Benkhettou, M. Badawi, A. Liang, J. Gonzalez and D. Errandonea, *J. Phys. Chem. C.*, 2021, **125**, 107. https://doi.org/10.1021/acs.jpcc.0c08641

15 J. P. Perdew, A. Ruzsinszky, G. I. Csonka, O. A. Vydrov, G. E. Scuseria, L. A. Constantin, X. Zhou and K. Burke, *Phys. Rev. Lett.*, 2008, **100**, 136406. https://doi.org/10.1103/PhysRevLett.100.136406

16 S. L. Dudarev, G. A. Botton, S. Y Savrasov, C. J Humphreys and A. P. Sutton, *Phys. Rev. B.*, 1998, **57**, 1505-1509. DOI:https://doi.org/10.1103/PhysRevB.57.1505

17 A. Togo and I. Tanaka, *Scripta. Mater.*, 2015, **108**, 1-5. https://doi.org/10.1016/j.scriptamat.2015.07.021

18 X. Gonze and C. Lee, *Phys. Rev. B.*, 1997, **55**, 10355. https://doi.org/10.1103/PhysRevB.55.10355

19 P. Giannozzi, S. de Gironcoli, P. Pavone and S. Baroni, *Phys. Rev. B.*, 1991, **43**, 7231. https://doi.org/10.1103/PhysRevB.43.7231

20 R. A. Boto, J. P. Piquemal and J. Contreras-García, *Theor. Chem. Acc.*, 2017, **136**, 139. https://hal.archives-ouvertes.fr/hal-01636270

21 E. R. Johnson, S. Keinan, P. Mori-Sanchez, J. Contreras-García, A. J. Cohen and W. Yang, *J. Am. Chem. Soc.*, 2010, **132**, 6498-6506. https://doi.org/10.1021/ja100936w

22 R. F. W. Bader, *Atoms in molecules: A quantum theory*, Oxford Clarendon Press, U. K., 1990.

23 T. Ouahrani, I. Merad-Boudia, H. Baltache, R. Khenata and Z. Bentalha, *Phys. Scr.*, 2011, **84**, 025704. https://doi.org/10.1088/0031-8949/84/02/025704

24 C. Keller. *Z. fur Anorg. Allg. Chem.*, 1962, **318**, 89-106. https://doi.org/10.1002/zaac.19623180108

25 F. Birch, *J. Geophys. Res.*, 1978, **83**, 1257-1268. https://doi.org/10.1029/JB083iB03p01257

26 L. Chen, M. Hu, J. Guo, X. Chong and J. Feng, *J. Mat. Science Techn.*, 2020, **52**, 20-28. https://doi.org/10.1016/j.jmst.2020.02.051

27 D. Errandonea and J. Ruiz-Fuertes, *Crystals.*, 2018, **8**, 71. https://doi.org/10.3390/cryst8020071

28 D. Errandonea, C. Popescu, A. B. Garg, P. Botella, D. Martinez-García, J. Pellicer-Porres, P. Rodríguez-Hernández, A. Muñoz, V. Cuenca-Gotor and J. A. Sans, *Phys. Rev. B.*, 2016, **93**, 035204. https://doi.org/10.1103/PhysRevB.93.035204

29 J. Feng, S. Shian, B. Xiao and D. R. Clarke, *Phys. Rev. B.*, 2014, **90**, 094102. https://doi.org/10.1103/PhysRevB.90.094102

30 D. Errandonea, R. Kumar, J. López-Solano, P. Rodríguez-Hernández, A. Muñoz, M. G. Rabie and R. Sáez Puche, *Phys. Rev. B.*, 2011, **83**, 134109. DOI:https://doi.org/10.1103/PhysRevB.83.134109

31 D. Errandonea, A. Muñoz, P. Rodríguez-Hernández, O. Gomis, S. Nagabhusan Achary, C. Popescu, S. J. Patwe and A. K. Tyagi, *Inorg. Chem.*, 2016, **55**, 4958–4969. https://doi.org/10.1021/acs.inorgchem.6b00503

32 T. Marqueño, D. Errandonea, J. Pellicer-Porres, D. Martinez-Garcia, D. Santamaria-Pérez, A. Muñoz, P. Rodríguez-Hernández, A. Mujica, S. Radescu, S. N. Achary, C. Popescu and M. Bettinelli, *Phys. Rev. B.*, 2019, **100**, 064106. https://doi.org/10.1103/PhysRevB.100.064106

33 M. Born and K. Huang, Ed., *Dynamical Theory and Experiment*, Springer, Berlin, 1982, vol. 1.

34 J. Fu, in *Density Functional Calculations: Recent Progresses of Theory and Application*, ed, G. Yang, IntechOpen, 2018, pp. 219-241. https://www.intechopen.com/chapters/58242. https://doi.org/10.5772/intechopen.72301

35 Z. J. Wu, E. J. Zhao, H. P. Xiang, X. F. Hao, X. J. Liu and J. Meng, *Phys. Rev. B.*, 2007, **76**, 054115. https://doi.org/10.1103/PhysRevB.76.054115

36 R. Gaillac, P. Pullumbi and F.-X. Coudert, *J. Phys. Condens. Matter.*, 2016, **28**, 275201-275206. https://doi.org/10.1088/0953-8984/28/27/275201

37 W. Voigt, *ed. Teubner*, 1928, Leipzig.

38 A. Reuss, *Z. Angew. Math. Mech.*, 1929, **9**, 49-58. https://doi.org/10.1002/zamm.19290090104

39 R. Hill, *Proc. Phys. Soc. A.*, 1952, **65**, 349. https://doi.org/10.1088/0370-1298/65/5/307

40 S. F. Pugh, *The London, Edinburgh, and Dublin Philosophical Magazine and Journal of Science*, 1954, **45**, 823–843. https://doi.org/10.1080/14786440808520496

41 M. Roknuzzaman, M. A. Hadi, M. A. Ali, M. M. Hossain, N. Jahan, M. M. Uddin, J. A. Alarco and K. Ostrikov, *J. Alloys Compd.*, 2017, **727**, 616-626. https://doi.org/10.1016/j.jallcom.2017.08.151

42 I. S. Elfimov, A. Rusydi, S. I. Csiszar, Z. Hu, H. H. Hsieh, H.-J. Lin, C. T. Chen, R. Liang and G. A. Sawatzky, *Phy. Rev. Lett.*, 2007, **98**, 137202. https://doi.org/10.1103/physrevlett.98.137202

43 T. Liu, X. Zhou, M. Dupuis and C. Li, *Phys. Chem. Chem. Phys.*, 2015, **17**, 23503. https://doi.org/10.1039/C5CP04299B

44 T. Ouahrani, I. Merad-Boudia, H. Baltache, R. Khenata, Z. Bentalha *Phys. Scr.*, **2011**, 84 025704. https://doi.org/10.1088/0031-8949/84/02/025704

45 H. Z. Guedda, T. Ouahrani, A. Morales-García, R. Franco, M. A. Salvadó, P. Pertierra and J. M. Recio, *Phys. Chem. Chem. Phys.*, 2016, **18**, 8132-8139. https://doi.org/10.1039/C6CP00081A